Dynamic force transmitted by hydraulic mount: Estimation in frequency domain using motion and/or pressure measurements and quasi-linear models

Jong-Yun Yoon[a] and Rajendra Singh[b]

(Received: 27 July 2009; Revised: 26 April 2010; Accepted: 28 April 2010)

This article proposes indirect methods to estimate dynamic forces that are transmitted by a fixed or free decoupler type hydraulic engine mount to a rigid base. First, the linear system transfer functions that relate the force transmitted to the top chamber pressure and excitation displacement are derived in the Laplace and frequency domains; these clearly identify the roles of rubber and hydraulic force paths up to 50 Hz. Since hydraulic mounts are inherently nonlinear, a quasi-linear model is developed that incorporates amplitude-sensitive and spectrally-varying parameters such as top chamber compliance and rubber path properties (stiffness and damping). Alternate schemes based on a quasi-linear fluid system formulation work well as dynamic force spectra over a range of harmonic displacement excitations are successfully predicted given motion and/or pressure measurements; these compare well with measured forces over a range of frequencies and excitation amplitudes. In particular, the force to pressure transfer function model is quite promising. Conversely, the analogous mechanical system model fails as it yields highly inaccurate forces. The force time history is also briefly predicted by applying the Fourier expansion with an embedded quasi-linear fluid model with only the fundamental (excitation) frequency. ***© 2010 Institute of Noise Control Engineering.***

Primary subject classification: 46.1; Secondary subject classification: 76.9

1 INTRODUCTION

Minimization of dynamic forces that are transmitted to rigid, compliant foundations in machines, vehicles and buildings is an important design paradigm in vibration and structure-borne noise control. Yet, the interfacial forces are difficult to measure using direct methods under realistic conditions[1–3]. Therefore, indirect methods must be utilized to estimate dynamic forces and moments using the internal states or motions of the isolation paths, vibration sources and receiving structures[1–5]. Further, most vibration isolators and machinery mounts are inherently nonlinear[6–8] and consequently improved system identification models are needed to assess forces from motion and/or internal state measurements. This article discusses this particular issue with application to hydraulic engine mounts that exhibit spectrally-varying and amplitude-sensitive properties[8–10].

The dynamic characteristics of hydraulic engine mounts have been examined using fluid and mechanical system models[9,11–23]. For instance, Singh et al.[11] analyzed the linear characteristics of both fixed and free decoupler mounts. Colgate et al.[12] examined the dynamic characteristics of hydraulic mount by employing equivalent linear models. Kim and Singh[13,14] found the nonlinear properties of chamber compliances and fluid resistances. Tiwari et al.[15] refined these measurements and defined the nonlinear characteristics of inertia track resistances and upper and lower chamber compliances over a range of the static preloads. Adiguna et al.[16] studied the transient responses under step and saw tooth excitations. He and Singh[9,17] compared the fluid and analogous mechanical system models and predicted the system responses in both time and frequency domains. Shangguan and Lu[18] calculated the dynamic fluid pressure in the upper chamber and investigated the influence of temperature on fluid

[a] Acoustics and Dynamics Laboratory, Department of Mechanical Engineering and Smart Vehicle Concepts Center The Ohio State University, Columbus, Ohio 43210, USA.

[b] Acoustics and Dynamics Laboratory, Department of Mechanical Engineering and Smart Vehicle Concepts Center The Ohio State University, Columbus, Ohio 43210, USA; email: singh.3@osu.edu.

(a)

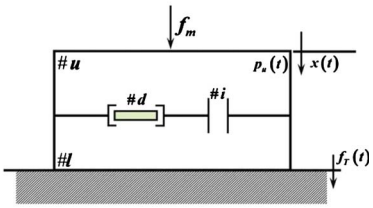

(b)

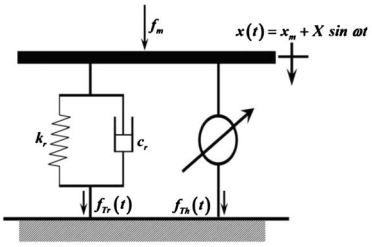

(c)

Fig. 1—Force transmitted $f_T(t)$ by a hydraulic mount in the context of non-resonant elastomeric test[18]: (a) experimental setup with mount; (b) schematic of the mount and measurements; (c) sinusoidal displacement excitation $x(t)$ and dynamic forces transmitted by two paths (f_{Tr} and f_{Th}).

viscosity. Fan and Lu[19] introduced a plate type mount and experimentally studied its function. Truong and Ahn[20] determined the performance of an inertia track with variable area using an analogous mechanical system model. Christopherson and Jaza[21] introduced a direct decoupler type mount and investigated its nonlinear model by comparing it with a floating decoupler type mount. Lee and Singh[22,23] have found superharmonics in the mount responses when excited harmonically and have suggested that vehicle system behavior would be nonlinear. Overall, none of the prior studies has examined the force measurement and related estimation issues which are the focus of this article.

2 PROBLEM FORMULATION

Figures 1 and 2 describe the experimental setup and hydraulic mount along with its fluid system in the context of non-resonant dynamic stiffness testing procedure under the ISO standard 10846[24]. Here, f_m is the preload; $x(t)=x_m+X \sin \omega_o t$ is the excitation displacement; x_m is the mean displacement; X is the excitation amplitude, but it is usually given in zero-to-peak[25]. In this test, the force transmitted to the

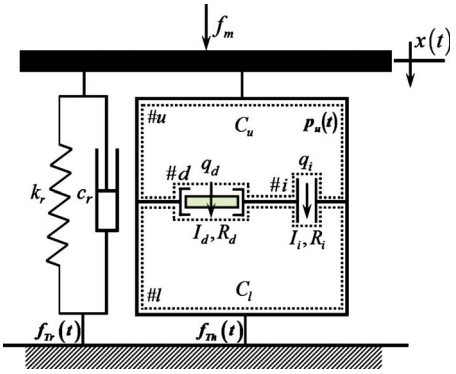

Fig. 2—Fluid model of the hydraulic mount and its parameters for rubber and hydraulic paths.

rigid base $f_T(t)$ is measured under sinusoidal excitation, though a Fourier filter is utilized to retain only the fundamental frequency signal[25]. Additionally, we install a pressure transducer in the upper chamber (in our laboratory experiments) and measure the dynamic pressure

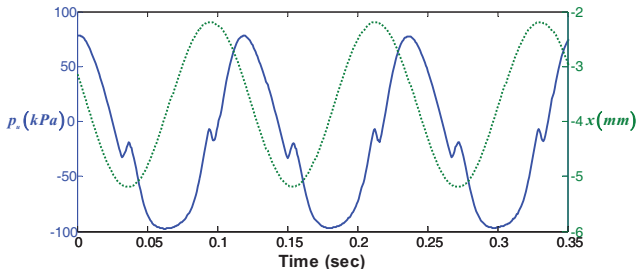

(a)

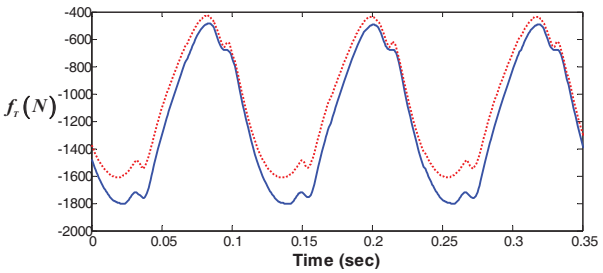

(b)

Fig. 3—Comparison between measured and predicted transmitted force time histories for the free decoupler mount, given sinusoidal displacement $x(t)=X \sin \omega_o t$ at $\omega_o/2\pi=8.5$ Hz and $X=1.5$ mm: (a) measured $x(t)$ with $X=1.5$ mm and $p_u(t)$ time histories; Key for part (a): ⋯ (green), $x(t)$; — (blue), $p_u(t)$; (b) measured and predicted force, $f_T(t)$; Key for part (b); — (blue), experiment; ⋯ (red), theory (Eqn. (1) given nominal parameters of Table 1).

Table 1—Nominal parameters for fluid and mechanical system models.

Force Path/ System Model		Parameters Symbols (units)	Nominal Value
Rubber Path (Figs. 1 and 2)		k_r (N/m)	2×10^5
		c_r (N-s/m)	496.1
Hydraulic Path	Fluid System Model (Figs. 1 and 2)	A_r (m^2)	4×10^{-3}
		I_i (kg/m^4)	4×10^6
		I_d (kg/m^4)	509.3
		C_u (m^5/N)	2.5×10^{-11}
		C_l (m^5/N)	2.4×10^{-9}
		R_i (N-s/m^5)	2×10^8
		R_d (N-s/m^5)	5×10^8
	Analogous Mechanical System Model (Fig. 11)	m_{ie} (kg)	81
		c_{ie} (N-s/m)	4.1×10^3
		k_u (N/m)	8.1×10^5
		k_l (N/m)	8.4×10^3

$p_u(t)$. The force transmitted $f_T(t)$ is related to the excitation displacement $x(t)$ and fluid system response $p_u(t)$ as shown below in both time (t) and frequency (ω) domains; here the uppercase symbols represent complex value Fourier amplitudes.

$$f_T(t) = f_{Tr}(t) + f_{Th}(t), \tag{1a}$$

$$f_{Tr}(t) = c_r\dot{x}(t) + k_r x(t), \tag{1b}$$

$$f_{Th}(t) = A_r p_u(t). \tag{1c}$$

$$F_T(\omega) = F_{Tr}(\omega) + F_{Th}(\omega), \tag{2a}$$

$$F_{Tr}(\omega) = (i\omega c_r + k_r)X(\omega), \tag{2b}$$

$$F_{Th}(\omega) = A_r P_u(\omega). \tag{2c}$$

Here, $f_{Tr}(t)$ is the force from the rubber path via rubber (subscript r); $f_{Th}(t)$ is the force from the hydraulic path (subscript h); k_r and c_r are the rubber stiffness and damping (using the Voight model), respectively; and A_r is the effective rubber (piston) area. Initially we assume a linear time-invariant system with nominal parameters, and thus only the sinusoidal responses at ω_o are considered in Eqns. (2a)–(2c).

First, we present some initial results to illustrate the nature of the problem. Consider a free decoupler mount (refer to Refs. 11 and 14–16 for a detailed description) under steady state sinusoidal excitation. Let us assume that we have both $x(t)$ and $p_u(t)$ signals under certain dynamic test conditions, and thus the measured $x(t)$ and $p_u(t)$ data set could be employed to estimate $f_T(t)$ and $F_T(\omega)$ by using Eqns. (1a)–(1c) and (2a)–(2c). Fig. 3 compares the time domain results at 8.5 Hz for this

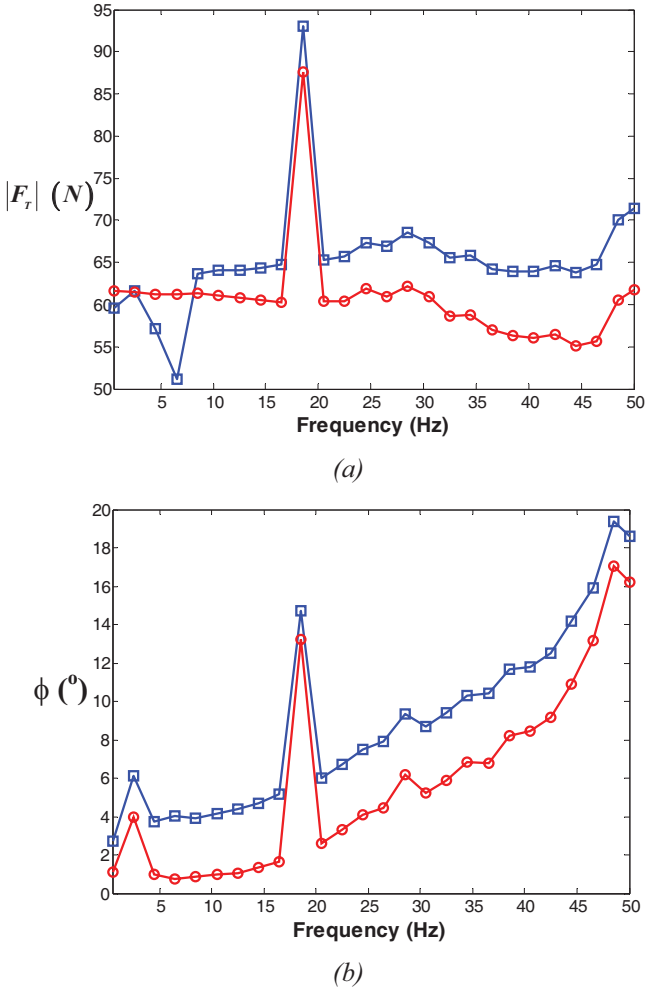

Fig. 4—Comparison between measured and predicted transmitted force, $f_T(t) = |F_T|\sin(\omega_o t + \phi)$ for the free decoupler mount given $X = 0.15$ mm: (a) magnitude spectra; (b) phase spectra. Key: ⊟ (blue), experiment; ⊖ (red), theory (Eqn. (2) given nominal parameters of Table 1).

particular mount given the nominal parameters of Table 1. Discrepancies between the prediction and the measurement are seen. Fig. 4 compares measured and estimated $F_T(\omega)$ for a low excitation level up to 50 Hz. Again we observe significant differences between the measured and estimated $F_T(\omega)$. Therefore, the force estimation method as given by Eqns. (1a)–(1c) and (2a)–(2c) must include the effective properties of the mounts and, in particular, their frequency ω_o and excitation amplitude X dependent properties for both rubber and hydraulic paths.

The current study will examine the hydraulic mount alone, with fixed or free decoupler design. Predictions of $f_T(t)$ and $F_T(\omega, X)$ will be based on fluid and analogous mechanical system models, and the results will be correlated with measured force signals from the

elastomer test machine. Only the steady state vertical displacements up to 50 Hz over a range of X from 0.15 to 1.5 mm (zero-to-peak) will be considered. This range of X corresponds to typical engine excitations. The specific objectives of this article are as follows: (1) determine the linear system transfer functions that relate F_T to X and P_u in the Laplace and frequency domains for both rubber and hydraulic force paths, and predict $f_T(t)$ using $x(t)$ and/or $p_u(t)$; (2) estimate the effective (frequency and amplitude dependent) mount parameters, and embed them in quasi-linear models. All mount nonlinearities will be lumped into upper chamber compliance $C_{ue}(\omega,X)$, rubber stiffness $k_r(\omega,X)$, and damping $c_r(\omega,X)$ properties; (3) estimate force $f_T(t)$ in the time domain by using the quasi-linear model and the Fourier expansion method, and compare sinusoidal force predictions with measurements. This study will consider only the fundamental harmonic (ω_o), like the dynamic stiffness measurements employed by the non-resonant elastomer test machines[25]. The quasi-linear model with effective $C_{ue}(\omega,X)$, $k_{re}(\omega,X)$ and $c_{re}(\omega,X)$ will be employed for such calculations.

3 FLUID SYSTEM MODEL: LINEAR SYSTEM ANALYSIS

3.1 Transfer Functions Relating Pressure and Displacement

A lumped model of the fluid system could be developed as illustrated in Figs. 1 and 2 based on the following assumptions: (1) the underlying system is a linear time-invariant and assigned with nominal fluid system parameters; (2) the mount is connected to a rigid base, and the top end is excited by the steady state sinusoidal displacement $x(t)$ under a mean load; (3) the force transmitted to the rigid base consists of two path forces. The momentum and continuity equations lead to the following governing equations and fluid parameters; they are well described in the literature[11,13–17,22,23].

$$p_u(t) - p_l(t) = I_i\dot{q}_i(t) + R_i q_i(t), \tag{3a}$$

$$p_u(t) - p_l(t) = I_d\dot{q}_d(t) + R_d q_d(t), \tag{3b}$$

$$C_u\dot{p}_u(t) = A_r\dot{x}(t) - q_i(t) - q_d(t), \tag{3c}$$

$$C_l\dot{p}_l(t) = q_i(t) + q_d(t). \tag{3d}$$

Here, C_u and C_l are the upper (#u) and lower (#l) chamber compliances, respectively; I_i and I_d are the inertances of the decoupler (#d) and inertia track (#i), respectively; R_i and R_d are the resistances of decoupler and inertia track, respectively; and q_d and q_i are the fluid flow through decoupler and inertia track, respectively. Transform Eqns. (1a)–(1c) and (3a)–(3d) into the Laplace domain (s) with the assumption that the initial conditions are zeros.

$$F_T(s) = F_{Tr}(s) + F_{Th}(s), \tag{4a}$$

$$F_{Tr}(s) = (c_r s + k_r)X(s), \tag{4b}$$

$$F_{Th}(s) = A_r P_u(s), \tag{4c}$$

$$P_u(s) - P_l(s) = (I_i s + R_i)Q_i(s), \tag{4d}$$

$$P_u(s) - P_l(s) = (I_d s + R_d)Q_d(s), \tag{4e}$$

$$C_u s P_u(s) = A_r s X(s) - Q_i(s) - Q_d(s), \tag{4f}$$

$$C_l s P_l(s) = Q_i(s) + Q_d(s). \tag{4g}$$

Note that $F_{Tr}(s)$ and $F_{Th}(s)$ in Eqns. (4b) and (4c) are the dynamic forces tranmitted by the rubber and hydraulic paths, respectively. Prior literature[9,11,14–16,22] has primarily focused on the dynamic stiffness formulation. We extend this concept further and examine other transfter functions. First consider the fixed decoupler mount. From Eqns. (4a)–(4g), the relationship between $P_u(s)$ and $X(s)$ is derived by assuming that $I_d = 0$ and $R_d \to \infty$:

$$\frac{P_u}{X}(s) = \frac{A_r(C_l I_i s^2 + C_l R_i s + 1)}{C_u C_l I_i s^2 + C_u C_l R_i s + (C_u + C_l)}. \tag{5a}$$

Next consider the free decoupler mount and assume that $I_d \approx 0$ below 50 Hz. Resulting transfer function is as follows:

$$\frac{P_u}{X}(s) = \frac{A_r[C_l I_i R_d s^2 + (C_l R_i R_d + I_i)s + (R_i + R_d)]}{C_u C_l I_i R_d s^2 + [C_u C_l R_i R_d + (C_u + C_l)I_i]s + (C_u + C_l)(R_i + R_d)}. \tag{5b}$$

Table 2—Fluid system parameters for fixed and free decoupler mounts assuming linear time-invariant system. Refer to Eqn.(6) and Fig. 5 for details.

Parameter	Fixed Decoupler	Free Decoupler
ζ_1	$\frac{1}{2}\sqrt{\frac{C_l R_i^2}{I_i}}$	$\frac{1}{2}\left(\sqrt{\frac{C_l R_d R_i^2}{I_i(R_i+R_d)}}+\sqrt{\frac{I_i}{C_l R_d(R_i+R_d)}}\right)$
ω_{N1} (rad/s)	$\sqrt{\frac{1}{C_l I_i}}$	$\sqrt{\frac{R_i+R_d}{C_l I_i R_d}}$
ζ_2	$\frac{1}{2}\sqrt{\frac{C_u C_l R_i^2}{I_i(C_u+C_l)}}$	$\frac{1}{2}\left[\sqrt{\frac{C_u C_l R_d R_i^2}{I_i(C_u+C_l)(R_i+R_d)}}+\sqrt{\frac{(C_u+C_l)I_i}{C_u C_l R_d(R_i+R_d)}}\right]$
ω_{N2} (rad/s)	$\sqrt{\frac{C_u+C_l}{C_u C_l I_i}}$	$\sqrt{\frac{(C_u+C_l)(R_i+R_d)}{C_u C_l I_i R_d}}$

Both transfer functions (now designated by $G(s)$), Eqns. (5a) and (5b), could be converted into a standard form as shown below:

$$\frac{P_u}{X}(s)=G(s)=\frac{A_r}{C_u+C_l}\frac{\frac{s^2}{\omega_{N1}^2}+\frac{2\zeta_1}{\omega_{N1}}s+1}{\frac{s^2}{\omega_{N2}^2}+\frac{2\zeta_2}{\omega_{N2}}s+1}. \tag{6}$$

Here, ζ_1 and ζ_2 are the damping ratios, and ω_{N1} and ω_{N2} are the natural frequencies of the numerator (zero of $G(s)$) and denominator (pole of $G(s)$). They are related to the fluid parameters for fixed and free decoupler mounts in Table 2. Note that the standard parameters are slightly different from the one reported previously since the previous study included the assumption that $C_l \geqslant 100 C_u$ (See Ref. 11). However, the current study does not include this assumption since the system might be affected by a variety of ranges of C_u while the quasi-linear model is applied with the effective value of C_u.

3.2 Dimensionless Formulations

We develop dimensionless formulations by using the following reference values: X_{ref}=reference excitation displacement amplitude; k_{rref}=reference stiffness; P_{uref} =reference pressure=$(k_{rref}X_{ref})/A_r$; and F_{Tref} =reference force=$k_{rref}X_{ref}$. With these reference values, define the dimensionless variables as follows.

$$\bar{X}=\frac{X}{X_{ref}}, \tag{7a}$$

$$\bar{P}_u(s)=\frac{A_r}{k_{rref}X_{ref}}P_u(s), \tag{7b}$$

$$\frac{\bar{P}_u}{\bar{X}}(s)=\bar{G}(s)=\frac{A_r}{k_{rref}}\frac{P_u}{X}(s), \tag{7c}$$

$$\frac{\bar{F}_T}{\bar{X}}(s)=\bar{K}(s)=\frac{1}{k_{rref}}\frac{F_T}{X}(s). \tag{7d}$$

where $\bar{K}(s)$ is the dimensionless cross point dynamic stiffness. In our work, we select the reference values, $k_{rref}=2.0\times10^5$ N/m, $A_r=4.5\times10^{-3}$ m^2, but X_{ref} ($\times10^{-3}$ m) is chosen according to the excitation amplitude used in experiments. By using Eqns. (6) and (7a)–(7d), we obtain the dimensionless $\bar{G}(s)$ as follows, where γ_h is the dimensionless static compliance resulting from the elastic containers of upper and lower chambers.

$$\bar{G}(s)=\frac{\bar{P}_u}{\bar{X}}(s)=\gamma_h\left(\frac{s^2}{\omega_{N1}^2}+\frac{2\zeta_1}{\omega_{N1}}s+1\right)\Bigg/\left(\frac{s^2}{\omega_{N2}^2}+\frac{2\zeta_2}{\omega_{N2}}s+1\right), \tag{8a}$$

$$\gamma_h=\frac{A_r^2}{k_{rref}(C_u+C_l)}. \tag{8b}$$

Further the dynamic stiffness $\bar{K}(s)$ and its rubber ($\bar{K}_r$) and hydraulic ($\bar{K}_h$) components are described using Eqns. (7d), (8a), and (8b).

$$\bar{K}(s)=\frac{\bar{F}_T}{\bar{X}}(s)=\frac{\bar{F}_{Tr}}{\bar{X}}(s)+\frac{\bar{F}_{Th}}{\bar{X}}(s), \tag{9a}$$

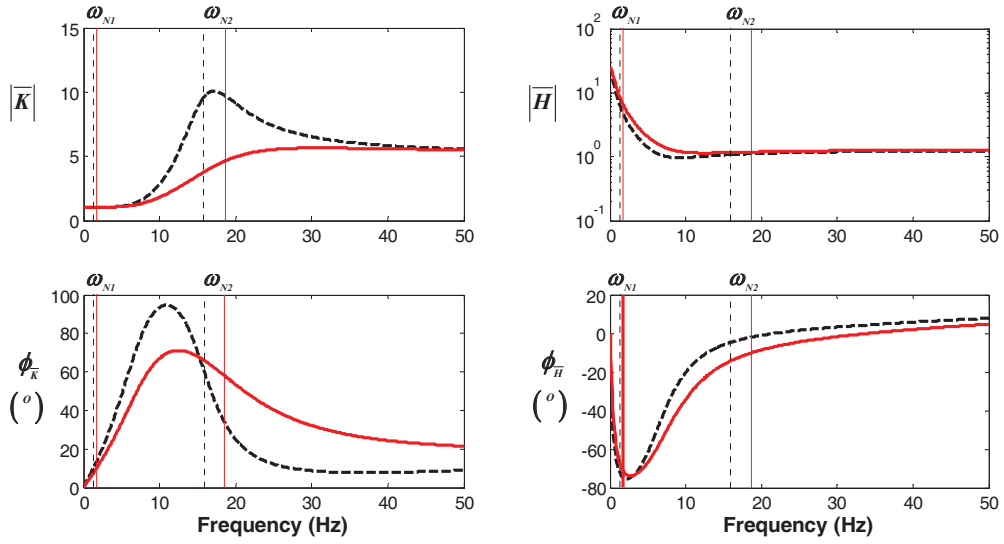

(a) (b)

Fig. 5—Typical frequency responses for fixed and free decoupler mounts based on linear system based formulation with nominal parameters as listed in Tables 1 and 2. Natural frequencies are identified here: (a) $|\bar{K}(\omega)| = |\bar{F}_T(\omega)/\bar{X}|$, $\phi_{\bar{K}} = \angle \bar{F}_T(\omega)/\bar{X}$; (b) $|\bar{H}(\omega)| = |\bar{F}_T(\omega)/\bar{P}_u|$, $\phi_{\bar{H}} = \angle \bar{F}_T(\omega)/\bar{P}_u$. Key: ⋯ (black), fixed decoupler mount; — (red), free decoupler mount.

$$\bar{K}_r(s) = \frac{\bar{F}_{Tr}}{\bar{X}}(s) = \gamma_r(1 + \tau_r s), \tag{9b}$$

$$\bar{K}_h(s) = \frac{\bar{F}_{Th}}{\bar{X}}(s) = \gamma_h\left(\frac{s^2}{\omega_{N1}^2} + \frac{2\zeta_1}{\omega_{N1}}s + 1\right) \Big/ \left(\frac{s^2}{\omega_{N2}^2} + \frac{2\zeta_2}{\omega_{N2}}s + 1\right), \tag{9c}$$

$$\tau_r = \frac{c_r}{k_r}, \tag{9d}$$

$$\gamma_r = \frac{k_r}{k_{rref}}. \tag{9e}$$

Here, τ_r is the time constant of the rubber path (modeled using the Voight model), and γ_r is the dimensionless static stiffness. From the relationship between Eqns. (8a) and (9a), relate dynamic force and upper chamber pressure as follows.

$$\bar{H}(s) = \frac{\bar{F}_T}{\bar{P}_u}(s) = \frac{\bar{F}_{Tr}}{\bar{P}_u}(s) + \frac{\bar{F}_{Th}}{\bar{P}_u}(s), \tag{10a}$$

$$\bar{H}_r(s) = \frac{\bar{F}_{Tr}}{\bar{P}_u}(s) = \frac{\gamma_r}{\gamma_h}(1 + \tau_r s)\left(\frac{s^2}{\omega_{N2}^2} + \frac{2\zeta_2}{\omega_{N2}}s + 1\right) \Big/ \left(\frac{s^2}{\omega_{N1}^2} + \frac{2\zeta_1}{\omega_{N1}}s + 1\right), \tag{10b}$$

$$\bar{H}_h(s) = \frac{\bar{F}_{Th}}{\bar{P}_u}(s) = 1. \tag{10c}$$

Note that $\bar{H}_r(s)$ and $\bar{H}_h(s)$ represent the rubber and hydraulic path transmissibilities as they relate the force transmitted (to the rigid base) to the interfacial force (inside the fluid system).

3.3 Typical Frequency Responses Based on Nominal Parameters

When the hydraulic mount is harmonically excited under steady state condition, the Laplace transfer functions can be converted to the frequency response functions by changing the variable s with $j\omega$ where j is the imaginary unit. Figures 5–8 show typical frequency responses, in terms of $\bar{K}_r(\omega)$ $(\bar{H}_r(\omega))$ and $\bar{K}_h(\omega)$ $(\bar{H}_h(\omega))$ and compare rubber and hydraulic path forces for both fixed and free decoupler mounts. Based on nominal parameters, natural frequencies ω_{N1} and ω_{N2} are found to be 1.62 (1.9) Hz and 16 (19) Hz for the fixed (free) decoupler mount. In particular, Figs. 5(a) and 5(b) illustrate the dynamic characteristics in terms of

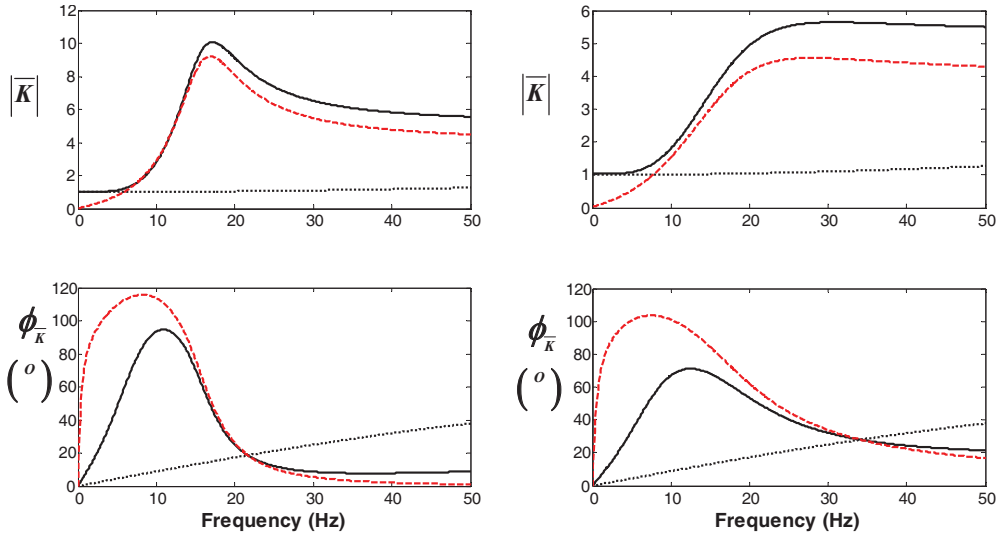

Fig. 6—Dynamic stiffness responses for rubber and hydraulic paths: (a) fixed decoupler mount; (b) free decouple mount. Key: — (black), $\bar{K}(\omega)=\bar{F}_T(\omega)/\bar{X}$; --- (red), $\bar{K}_h(\omega)=\bar{F}_{Th}(\omega)/\bar{X}$; ···, $\bar{K}_r(\omega)=\bar{F}_{Tr}(\omega)/\bar{X}$.

$\bar{K}(\omega)$ and $\bar{H}(\omega)$ respectively. As illustrated in Figs. 5(a) and 5(b), the system shows that the peak loss angle is located between ω_{N1} and ω_{N2} as suggested by prior research[11].

Figures 6 and 7 compare $\bar{K}_r(\omega)$ ($\bar{H}_r(\omega)$) from the rubber path with those from the hydraulic path $\bar{K}_h(\omega)$ ($\bar{H}_h(\omega)$). Figure 6 shows that hydraulic path magnitudes and loss angles are much higher than those from the rubber path forces (magnitudes are nearly constant, and the loss angles change linearly with the frequency). On the other hand, Fig. 7 shows that the rubber path forces, in terms of $\bar{H}_r(\omega)$, exhibit significant changes below 30 Hz. Overall, these curves suggest that the dynamic force transmitted is controlled by the hydraulic path. This could be confirmed by examining Eqns. (9a)–(9e) and (10a)–(10c). For example, Eqns. (9c) and

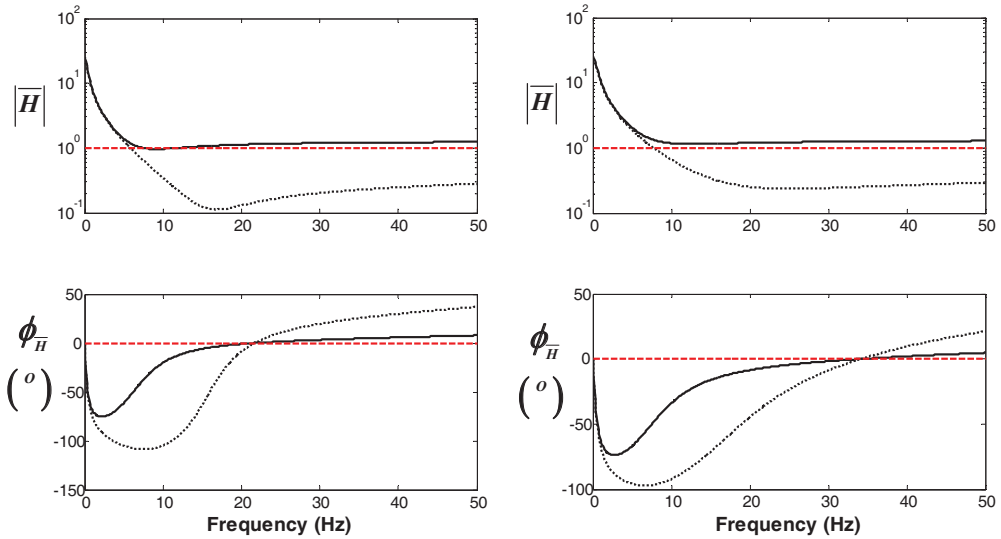

Fig. 7—Force transmissibilities for rubber and hydraulic paths: (a) fixed decoupler mount; (b) free decoupler mount. Key: — (black), $\bar{H}(\omega)=\bar{F}_T(\omega)/\bar{P}_u$; --- (red), $\bar{H}_h(\omega)=\bar{F}_{Th}(\omega)/\bar{P}_u$; ···, $\bar{H}_r(\omega)=\bar{F}_{Tr}(\omega)/\bar{P}_u$.

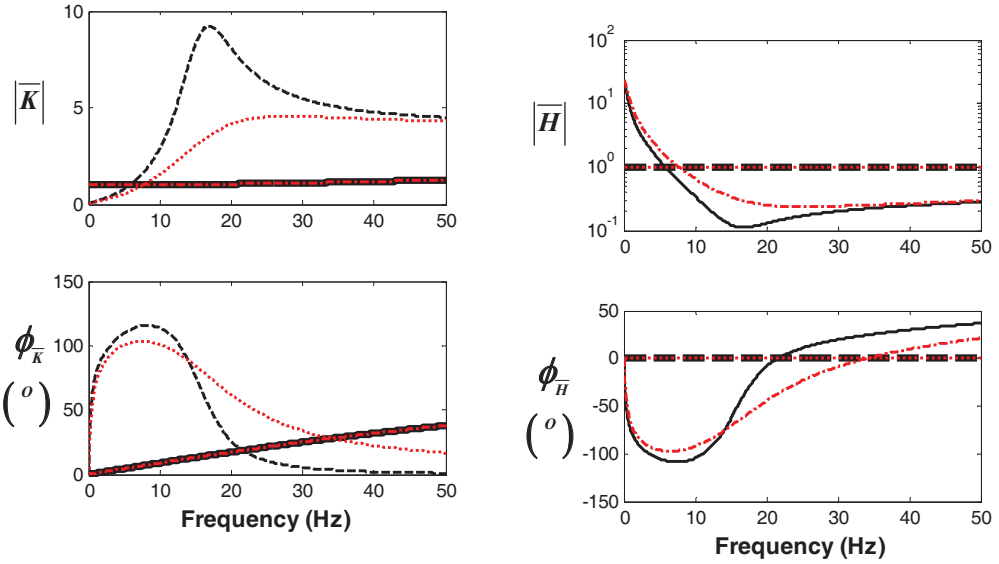

Fig. 8—Dynamic stiffness and force transmissibility responses for rubber and hydraulic paths: (a) $\bar{K}(\omega) = \bar{F}_T(\omega)/\bar{X}$; (b) $\bar{H}(\omega) = \bar{F}_T(\omega)/\bar{P}_u$. Key: — (black), $\bar{K}_r(\omega) = \bar{F}_{Tr}(\omega)/\bar{X}$ and $\bar{H}_r(\omega) = \bar{F}_{Tr}(\omega)/\bar{P}_u$ with fixed decouple mount; -·- (red), $\bar{K}_r(\omega) = \bar{F}_{Tr}(\omega)/\bar{X}$ and $\bar{H}_r(\omega) = \bar{F}_{Tr}(\omega)/\bar{P}_u$ with free decoupler mount; --- (black), $\bar{K}_h(\omega) = \bar{F}_{Th}(\omega)/\bar{X}$ and $\bar{H}_h(\omega) = \bar{F}_{Th}(\omega)/\bar{P}_u$ with fixed decoupler mount; ··· (red), $\bar{K}_h(\omega) = \bar{F}_{Th}(\omega)/\bar{X}$ and $\overline{H_h}(\omega) = \bar{F}_{Th}(\omega)/\bar{P}_u$ with free decoupler mount.

(10b) include fluid parameters in terms of ζ_1, ζ_2, ω_{N1}, and ω_{N2} (as described in Table 2). However, Eqns. (9b) and (10c) contain only the rubber path parameters, and these are nearly frequency-invariant. Figure 8 illustrates the contributions of $\bar{F}_{Tr}(\omega)$ and $\bar{F}_{Th}(\omega)$ in terms of $\bar{K}_r(\omega)$ ($\bar{H}_r(\omega)$) and $\bar{K}_h(\omega)$ ($\bar{H}_h(\omega)$). The comparisons show that the hydraulic path, below 30 Hz, affects the dynamic force $\bar{F}_T(\omega)$ more than the rubber path. However, the loss angle from the rubber path becomes more dominant beyond 30 Hz. These features also could be assessed by comparing $\bar{K}_r(\omega)$ and $\bar{H}_r(\omega)$ with $\bar{K}_h(\omega)$ and $\bar{H}_h(\omega)$ in Figs. 6 and 7.

4 SPECTRALLY-VARYING AND AMPLITUDE-SENSITIVE PROPERITIES

4.1 Effective Upper Chamber Compliance

The transfer functions of Sec. 3 are given for a linear system, but the hydraulic mount is a nonlinear device[13–17,22,23]. Thus, we must develop a quasi-linear model that would include effective properties. We assume that the upper chamber pressure is most affected by the nonlinear phenomena, and thus, all nonlinearities are lumped into the effective upper chamber compliance $C_{ue}(\omega,X)$. The definition of $C_{u\mathbf{n}}$ (compliance under nominal conditions for a linear device) is now changed, and the term $C_{ue}(\omega,X)$ is now a complex value parameter that includes both amplitude-sensitive stiffness and damping properties at any frequency. Define it using the empirical λ_u ($=\alpha + i\beta$) as follows, where the coefficients α and β would be determined from measurements:

$$C_{ue} = \lambda_u C_{u\mathbf{n}} = (\alpha + i\beta) C_{u\mathbf{n}}. \tag{11}$$

Then, C_u term of Eqn. (5a) for the fixed decoupler is replaced by C_{ue} to determine α and β as a function of ω and X. First, the measured $P_{uM}(\omega,X)$ dataset is defined (under sinudodal exciation) in terms of magitude P_{uM} and its phase ϕ_M as:

$$P_{uM} = P_{u\mathbf{RE}} + iP_{u\mathbf{IM}}, \tag{12a}$$

$$P_{u\mathbf{RE}} = Re(P_{uM}) = |P_{uM}|cos(\phi_M), \tag{12b}$$

$$P_{u\mathbf{IM}} = Im(P_{uM}) = |P_{uM}|sin(\phi_M). \tag{12c}$$

Then, Eqn. (5a) is expressed in the frequency domain as follows:

$$P_u(\omega,X) = \frac{A_r[(1-\omega^2 C_l I_i) + i\omega C_l R_i]X}{(C_u + C_l - \omega^2 C_u C_l I_i) + i\omega C_u C_l R_i}. \tag{13}$$

Thus, the coefficients α and β are estimated by substituting Eqns. (11) and (12a)–(12c) into Eqn. (13). These

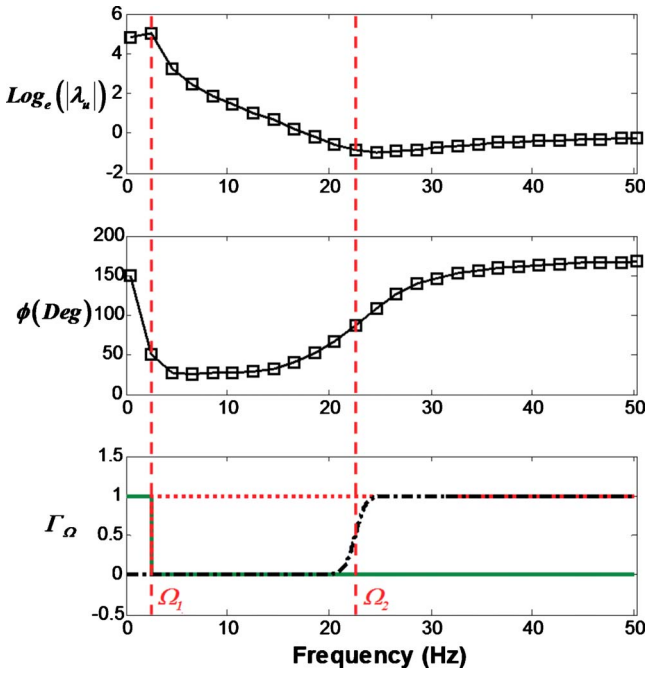

Fig. 9—Magnitude (on $\log_e$ scale) and phase curves of $\lambda_u(\omega,X)$ for fixed decoupler mount at $X=0.15$ mm, smoothening functions, Γ_Ω, and frequency regimes defined by $\Omega_1=2.5$ Hz and $\Omega_2=22.5$ Hz. Key for Γ_Ω curves:—(green), $\Gamma_{\Omega1}(\omega)$; ··· (red), $\Gamma_{\Omega2}(\omega)$; -·- (black), $\Gamma_{\Omega3}(\omega)$.

formulations will be investigated further in a companion paper; that article would determine superharmonics in the upper chamber pressure and force signals under sinusoidal excitation[26].

4.2 Procedures Used to Find $\lambda_u(\omega,X)$ Curve-Fits

By using the equations of Sec. 4.1 and measured $P_{uM}(\omega,X)$, we can calculate $\lambda_u(\omega,X)$ values. This discrete data set is curve-fit using piecewise polynomial functions and smoothened using hyper-tangent functions[27], as described next, in order to obtain continuous functions of the frequency for modeling purposes. Sample results are first illustrated in Fig. 9, where three frequency regimes are shown along with their smoothening functions. Although only one example of the magnitude and phase curves is shown in Fig. 9, the entire range of $\lambda_u(\omega,X)$ dependent upon X should be considered. Steps are described below.

First, the magnitude and phase of $\lambda_u(\omega,X)$ are grouped in three frequency regimes. A linear function is assumed to curve-fit below Ω_1 (=2.5 Hz); a 6th order polynomial function is chosen to define the curves between Ω_1 and Ω_2 (=22.5 Hz); and, a 4th order polynomial function is utilized above Ω_2 as illustrated in Fig. 9. Second, each polynomial function is multiplied by the relevant smoothening functions ($\Gamma_{\Omega1}(\omega)$, $\Gamma_{\Omega2}(\omega)$ and $\Gamma_{\Omega3}(\omega)$). The product of the smoothening function and the polynomial function yields the continuous $\lambda_u(\omega,X)$. Third, when $|\lambda_u(\omega,X)|$ is estimated in the frequency domain, it is on the log_e scale since the frequency responses of $|F_T(\omega,X)|$ are sensitive to a variation in $|\lambda_u(\omega,X)|$. The following expressions describe the polynomial functions, $\kappa_v(\omega)$ ($v=1-3$), of $|\lambda_u(\omega,X)|$ for three frequency regimes and their smoothening functions $\Gamma_{\Omega v}(\omega)$. These are functions of Ω ($=\omega/2\pi$, Hz).

$$\kappa_1(\omega)=a_{\kappa1}(\omega/2\pi)+a_{\kappa0},\quad \Omega<\Omega_1, \tag{14a}$$

$$\kappa_2(\omega)=b_{\kappa6}(\omega/2\pi)^6+b_{\kappa5}(\omega/2\pi)^5+b_{\kappa4}(\omega/2\pi)^4+b_{\kappa3}(\omega/2\pi)^3+b_{\kappa2}(\omega/2\pi)^2+b_{\kappa1}(\omega/2\pi)+b_{\kappa0},\quad \Omega_1<\Omega<\Omega_2, \tag{14b}$$

$$\kappa_3(\omega)=c_{\kappa4}(\omega/2\pi)^4+c_{\kappa3}(\omega/2\pi)^3+c_{\kappa2}(\omega/2\pi)^2+c_{\kappa1}(\omega/2\pi)+c_{\kappa0},\quad \Omega>\Omega_2, \tag{14c}$$

$$\Gamma_{\Omega1}(\omega)=0.5\{-tanh[\sigma_1(\omega/2\pi-\Omega_1)]+1\}, \tag{14d}$$

$$\Gamma_{\Omega2}(\omega)=0.5\{tanh[\sigma_2(\omega/2\pi-\Omega_1)]+1\}, \tag{14e}$$

$$\Gamma_{\Omega3}(\omega)=0.5\{tanh[\sigma_3(\omega/2\pi-\Omega_2)]+1\}. \tag{14f}$$

The following smoothening factors σ_v ($v=1-3$) are selected: $\sigma_1=1\times10^6$; $\sigma_2=1\times10^6$; and $\omega_3=1$. By applying this method, the entire set of coefficients (at each X) is estimated. For example, the coefficients for the fixed decoupler are as follows: $a_{\kappa1}=0.12$, 0.10, −0.06, −0.14, −0.29, −0.43 and −0.55 with $X=0.15$, 0.25, 0.5, 0.75, 1.0, 1.25 and 1.5 mm respectively. Also, $a_{\kappa0}=4.76$, 4.71, 4.93, 5.01, 5.31, 5.52 and 5.62 with $X=0.15$, 0.25, 0.5, 0.75, 1.0, 1.25 and 1.5 mm respectively. Further, curve-fit the coefficients in terms of X as suggested below.

$$a_{\kappa v}(X)=\sum_{w=1}^{7}a_{\kappa vw}X^{w-1}(v=0,1), \tag{15a}$$

$$b_{\kappa v}(X)=\sum_{w=1}^{7}b_{\kappa vw}X^{w-1}(v=0-5), \tag{15b}$$

$$c_{\kappa v}(X)=\sum_{w=1}^{7}c_{\kappa vw}X^{w-1}(v=0-4), \tag{15c}$$

$$a_{\kappa1}(X)=a_{\kappa16}X^6+a_{\kappa15}X^5+a_{\kappa14}X^4+a_{\kappa13}X^3+a_{\kappa12}X^2+a_{\kappa11}X+a_{\kappa10}. \tag{15d}$$

Here, $a_{\kappa v}(X)$, $b_{\kappa v}(X)$ and $c_{\kappa v}(X)$ are the coefficient functions. Index w in Eqns. (15a)–(15c) indicates

different X values since the experimental values of X are given for 7 cases only (X=0.15, 0.25, 0.5, 0.75, 1.0, 1.25 and 1.5 mm). Therefore, the coefficient polynomial functions are limited by the 6th order term as illustrated by Eqn. (15d). The estimated coefficients for Eqn. (15d) are: $a_{\kappa 16}=-6.63$; $a_{\kappa 15}=32.67$; $a_{\kappa 14}=-62.29$; $a_{\kappa 13}=57.76$; $a_{\kappa 12}=-26.86$; $a_{\kappa 11}=5.30$; and $a_{\kappa 10}=-0.24$. Using this method, all coefficients as a function of X are found. Therefore, $|\lambda_u(\omega,X)|$ is described in a continuous manner in terms of ω and X. The phase of $\lambda_u(\omega,X)$ is also described in the same way. In order to determine the values of $|\lambda_u(\omega,X)|$, the estimates are calibrated in terms of an exponential function since the empirical values of $|\lambda_u(\omega,X)|$ are curve-fit on a log_e scale. Therefore, the procedure to determine a continuous $|\lambda_u(\omega,X)|$ is summarized as follows:

$$|\lambda_u(\omega,X)| = e^{\kappa_{1e}(\omega,X)}, \tag{16a}$$

$$\kappa_{1e}(\omega,X) = \kappa_{\Omega 1}(\omega,X) + \kappa_{\Omega 2}(\omega,X) + \kappa_{\Omega 3}(\omega,X), \tag{16b}$$

$$\kappa_{\Omega 1}(\omega,X) = \kappa_{X1}(\omega,X)\Gamma_{\Omega 1}(\omega), \tag{16c}$$

$$\kappa_{\Omega 2}(\omega,X) = \kappa_{X2}(\omega,X)[\Gamma_{\Omega 2}(\omega) - \Gamma_{\Omega 3}(\omega)], \tag{16d}$$

$$\kappa_{\Omega 3}(\omega,X) = \kappa_{X3}(\omega,X)\Gamma_{\Omega 3}(\omega), \tag{16e}$$

$$\kappa_{X1}(\omega,X) = a_{\kappa 1}(X)(\omega/2\pi) + a_{\kappa 0}(X), \tag{16f}$$

$$\kappa_{X2}(\omega,X) = b_{\kappa 6}(X)(\omega/2\pi)^6 + b_{\kappa 5}(X)(\omega/2\pi)^5 + b_{\kappa 4}(X) \times(\omega/2\pi)^4 + b_{\kappa 3}(X)(\omega/2\pi)^3 + b_{\kappa 2}(X) \times(\omega/2\pi)^2 + b_{\kappa 1}(X)(\omega/2\pi) + b_{\kappa 0}(X), \tag{16g}$$

$$\kappa_{X3}(\omega,X) = c_{\kappa 4}(X)(\omega/2\pi)^4 + c_{\kappa 3}(X)(\omega/2\pi)^3 + c_{\kappa 2}(X) \times(\omega/2\pi)^2 + c_{\kappa 1}(X)(\omega/2\pi) + c_{\kappa 0}(X). \tag{16h}$$

Here, $\kappa_{1e}(\omega,X)$ is $log_e|\lambda_u(\omega,X)|$, $\kappa_{\Omega v}(\omega,X)$ (v=1−3) is the smoothened function of $\kappa_{Xv}(\omega,X)$ (v=1−3), $\kappa_{Xv}(\omega,X)$ (v=1−3) is the polynomial function over relevant frequency range with coefficient functions $a_{\kappa v}(X)$ (v=1−3), $b_{\kappa v}(X)$ (v=1−6), and $c_{\kappa v}(X)$ (v=1−4) as described by Eqns. (15a)–(15d). The smoothening functions $\Gamma_{\Omega v}(\omega)$ (v=1−3) are given by Eqns. (14d)–(14f).

The phase of $\lambda_u(\omega,X)$ is also determined as follows:

$$\varphi_{1e}(\omega,X) = \varphi_{\Omega 1}(\omega,X) + \varphi_{\Omega 2}(\omega,X) + \varphi_{\Omega 3}(\omega,X), \tag{17a}$$

$$\varphi_{\Omega 1}(\omega,X) = \varphi_{X1}(\omega,X)\Gamma_{\Omega 1}(\omega), \tag{17b}$$

$$\varphi_{\Omega 2}(\omega,X) = \varphi_{X2}(\omega,X)[\Gamma_{\Omega 2}(\omega) - \Gamma_{\Omega 3}(\omega)], \tag{17c}$$

$$\varphi_{\Omega 3}(\omega,X) = \varphi_{X3}(\omega,X)\Gamma_{\Omega 3}(\omega), \tag{17d}$$

$$\varphi_{X1}(\omega,X) = a_{\varphi 1}(X)(\omega/2\pi) + a_{\varphi 0}(X), \tag{17e}$$

$$\varphi_{X2}(\omega,X) = b_{\varphi 6}(X)(\omega/2\pi)^6 + b_{\varphi 5}(X)(\omega/2\pi)^5 + b_{\varphi 4}(X) \times(\omega/2\pi)^4 + b_{\varphi 3}(X)(\omega/2\pi)^3 + b_{\varphi 2}(X) \times(\omega/2\pi)^2 + b_{\varphi 1}(X)(\omega/2\pi) + b_{\varphi 0}(X), \tag{17f}$$

$$\varphi_{X3}(\omega,X) = c_{\varphi 4}(X)(\omega/2\pi)^4 + c_{\varphi 3}(X)(\omega/2\pi)^3 + c_{\varphi 2}(X) \times(\omega/2\pi)^2 + c_{\varphi 1}(X)(\omega/2\pi) + c_{\varphi 0}(X). \tag{17g}$$

Here, $\varphi_{1e}(\omega,X)$ is the phase of $\lambda_u(\omega,X)$, $\Gamma_{\Omega v}(\omega,X)$ (v=1−3) is the smoothened function of $\varphi_{Xv}(\omega,X)$ (v=1−3), $\varphi_{Xv}(\omega,X)$ (v=1−3) is the polynomial function for relevant frequency range with coefficient functions $a_{\varphi v}(X)$ (v=1−3), $b_{\varphi v}(X)$ (v=1−6), and $c_{\varphi v}(X)$ (v=1−4). The coefficients are also calculated using the method described by Eqns. (15a)–(15d).

4.3 Effective Rubber Path Properties

The linear system study of Sec. 3 has suggested the importance of both force paths, and therefore, we define effective rubber path properties as $C_{ue}(\omega,X)$. The effective stiffness $k_{re}(\omega,X)$ is defined as $k_{r\mathbf{n}}\lambda_{kr}(\omega,X)$, and $c_{re}(\omega,X)$ as $c_{r\mathbf{n}}\lambda_{cr}(\omega,X)$ where $k_{r\mathbf{n}}$ and $c_{r\mathbf{n}}$ are the nominal (linear system) values of k_r and c_r, respectively. $\lambda_{kr}(\omega,X)$ and $\lambda_{cr}(\omega,X)$ are spectrally-varying and amplitude-sensitive parameters for k_r and c_r, respectively[10]. Figure 10 shows the measured dynamic stiffness data from the rubber mount test with X=0.15 mm; this test is done when fluid is drained from the hydraulic mount. Thus, this represents the combined effect of the elastomeric parts within the mount. The methods of Sec. 4.2 are applied to obtain the continuous curve-fit schemes of $\lambda_{kr}(\omega,X)$ and $\lambda_{cr}(\omega,X)$. This issue will be further investigated in a companion article[26].

5 DYNAMIC FORCE ESTIMATION USING QUASI-LINEAR SYSTEM MODELS

The quasi-linear models with effective parameters in terms of $\lambda_u(\omega,X)$, $\lambda_{kr}(\omega,X)$, and $\lambda_{cr}(\omega,X)$ will be employed next to estimate $F_T(\omega,X)$ in the frequency domain by using Eqns. (2a)–(2c), (9a)–(9e), and (10a)–(10c). Also, alternate force estimation methods will be compared.

5.1 Analogous Mechanical System Model

Figure 11 illustrates the analogous mechanical system model which has the following equivalent parameters that are converted from the fluid system model: Effective mass of inertia track fluid column $m_{ie}=A_r^2 I_i$; effective viscous damping of inertia track fluid $c_{ie}=A_r^2 R_i$; equivalent stiffness of upper chamber

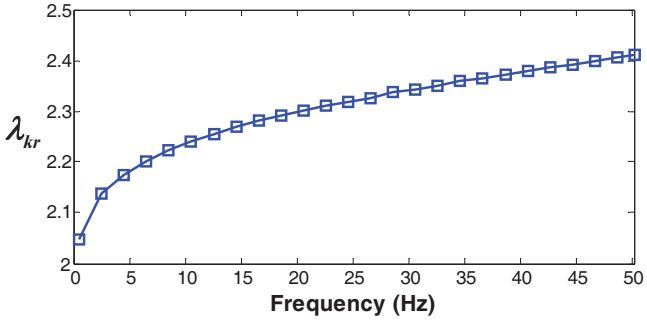

(a)

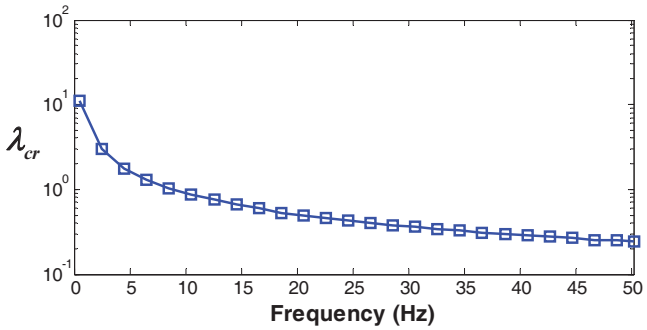

(b)

Fig. 10—Spectrally-varying and amplitude-sensitive properties of the rubber path with $X=0.15$ mm: (a) effective stiffness quantified by λ_{kr} ($=k_{re}/k_{rn}$) and displayed on a linear scale; (b) viscous damping quantified by λ_{cr} ($=c_{re}/c_{rn}$) and displayed on a $\log_e$ scale.

compliance $k_u=A_r^2/C_u$; and equivalent stiffness of lower chamber compliance $k_l=A_r^2/C_l$. The nominal values are listed in Table 1. As illustrated in Fig. 11, relationship between $x(t)$, $x_{ie}(t)$ and $f_T(t)$ is derived as follows:

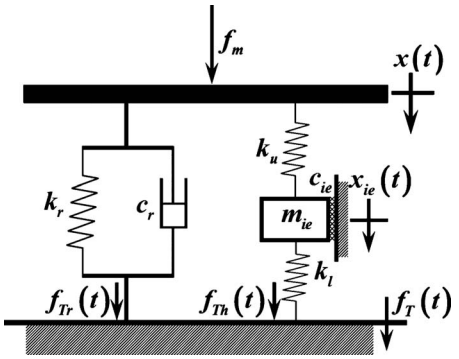

Fig. 11—Analogous mechanical system model and its parameters for rubber and hydraulic paths.

$$m_{ie}\ddot{x}_{ie}(t)+c_{ie}\dot{x}_{ie}(t)+(k_u+k_l)x_{ie}(t)=k_u x(t). \quad (18)$$

$$f_T(t)=c_r\dot{x}(t)+k_r x(t)+k_l x_{ie}(t). \quad (19)$$

where effective velocity of inertia track fluid is given by $\dot{x}_{ie}(t)=q_i(t)/A_r$. By taking the Laplace transform for both Eqns. (18) and (19), the transfer function of the hydraulic path, $F_{Ah}(s)/X(s)=N(s)$ is derived as follows:

$$X_{ie}(s)=\frac{k_u}{m_{ie}s^2+c_{ie}s+k_u+k_l}X(s). \quad (20)$$

$$\frac{F_T}{X}(s)=K_A(s)=\frac{F_{Ar}}{X}(s)+\frac{F_{Ah}}{X}(s), \quad (21a)$$

$$\frac{F_{Ar}}{X}(s)=(c_r s+k_r), \quad (21b)$$

$$\frac{F_{Ah}}{X}(s)=N(s)=\frac{k_u k_l}{m_{ie}s^2+c_{ie}s+k_u+k_l}. \quad (21c)$$

Also, the dimensionless dynamic stiffness $\bar{K}_A(s)$ is acquired by employing Eqns. (7a)–(7d) as follows:

$$\frac{\bar{F}_T}{\bar{X}}(s)=\bar{K}_A(s)=\frac{\bar{F}_{Ar}}{\bar{X}}(s)+\frac{\bar{F}_{Ah}}{\bar{X}}(s), \quad (22a)$$

$$\frac{\bar{F}_{Ar}}{\bar{X}}(s)=\gamma_r(1+\tau_r s), \quad (22b)$$

$$\frac{\bar{F}_{Ah}}{\bar{X}}(s)=\bar{N}(s)=\gamma_h \Big/ \left(\frac{s^2}{\omega_{N2}^2}+\frac{2\zeta_2}{\omega_{N2}}s+1\right). \quad (22c)$$

where $\bar{F}_{Ar}(s)/\bar{X}(s)$ formulation is the same as Eqn. (9a) and (9b). However, it differs from Eqn. (8a) as shown in Eqn. (22c).

5.2 Alternate Transfer Function Schemes

Alternate transfer function schemes, from Eqns. (2a)–(2c), (9a)–(9c), (10a)–(10c), and (22a)–(22c), could be considered along with quasi-linear model of Sec. 4. Table 3 lists alternate schemes (and their designations) as well as the type of measured data such as $X(\omega)$ and/or $P_u(\omega,X)$. Note that Schemes I, II, III, and IV are based on Eqn. (2a)–(2c), (9a)–(9c), (10a)–(10c), and (22a)–(22c) respectively whereas Scheme I is the simplest estimation of $\bar{F}_T(\omega,X)$ with Eqn. (2a)–(2c). In particular, Scheme III illustrates the direct relationship between $\bar{F}_T(\omega,X)$ and $\bar{P}_u(\omega,X)$ and Scheme IV employs the mechanical system parameters. The proposed schemes can incorporate spectrally-varying

Table 3—Comparison of alternate force estimation schemes based on quasi-linear system model

Scheme Designation		Sensor(s) required		Spectrally-varying and amplitude-sensitive parameters
		X	P_u	
Fluid System Model (Figs. 1 and 2)	*I-A*	Yes	Yes	$\lambda_{kr}=1, \lambda_{cr}=1$
	I-B	Yes	Yes	$\lambda_{kr}\neq 1, \lambda_{cr}\neq 1$
	II-A	Yes	No	$\lambda_{kr}=1, \lambda_{cr}=1, \lambda_u\neq 1$
	II-B	Yes	No	$\lambda_{kr}\neq 1, \lambda_{cr}\neq 1, \lambda_u=1$
	II-C	Yes	No	$\lambda_{kr}\neq 1, \lambda_{cr}\neq 1, \lambda_u\neq 1$
	III-A	No	Yes	$\lambda_{kr}=1, \lambda_{cr}=1, \lambda_u\neq 1$
	III-B	No	Yes	$\lambda_{kr}\neq 1, \lambda_{cr}\neq 1, \lambda_u=1$
	III-C	No	Yes	$\lambda_{kr}\neq 1, \lambda_{cr}\neq 1, \lambda_u\neq 1$
Analogous Mechanical System Model (Fig. 11)	*IV-A*	Yes	No	$\lambda_{kr}=1, \lambda_{cr}=1, \lambda_u\neq 1$
	IV-B	Yes	No	$\lambda_{kr}\neq 1, \lambda_{cr}\neq 1, \lambda_u=1$
	IV-C	Yes	No	$\lambda_{kr}\neq 1, \lambda_{cr}\neq 1, \lambda_u\neq 1$

and amplitude-sensitive parameters $\lambda_v(s;X)$ $(v=u,kr,cr)$ under harmonic excitation with amplitude X. In the limiting cases when $\lambda_v(s;X)=1$ $(v=u,kr,cr)$, the $\bar{F}_T(\omega,X)$ is estimated by the linear model with only nominal values. The proposed schemes (I, II, III and IV) are summarized in Fig. 12, via the block diagrams in Laplace domain including the sub-blocks that dictate $\bar{K}(s)$, $\bar{H}(s)$, and $\bar{K}_A(s)$. Therefore, the steady state responses are examined by changing the s term to $j\omega$. Scheme I of Fig. 12(a) and Table 3 is the simplest case though it needs both X and P_u measurements. By comparing the alternate schemes, the merits of each method could be considered in terms of the number of sensors needed and main transfer function such as $\bar{K}(s)$ or $\bar{H}(s)$.

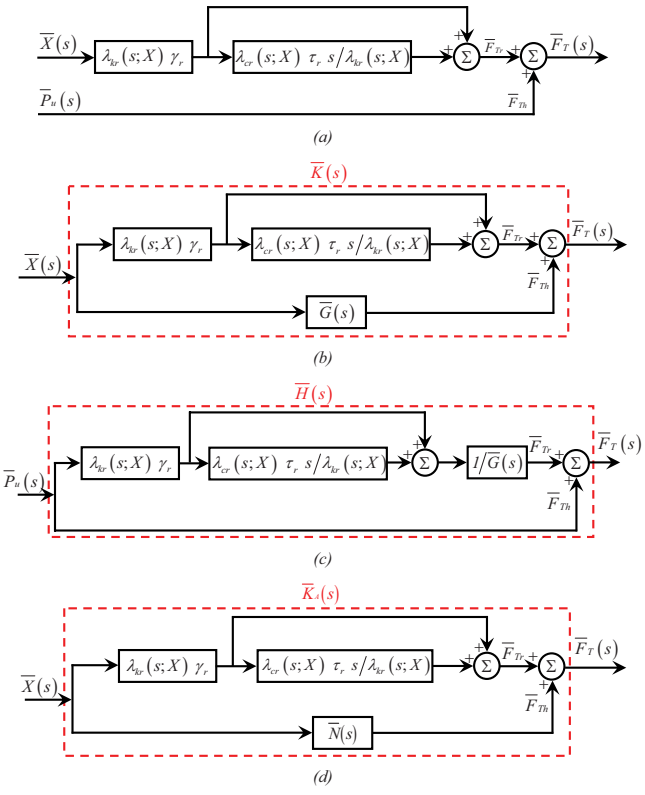

Fig. 12—Comparison of alternate schemes via block diagrams: (a) Scheme I; (b) Scheme II; (c) Scheme III; (d) Scheme IV.

5.3 Estimation of $\bar{F}_T(\omega,X)$ by Using Quasi-Linear Model

Figures 13 and 14 compare the results of both linear and quasi-linear models with experiment. Observe that the estimated dimensionless force is nearly equal to 2 when $\omega\rightarrow 0$ since the contribution of the hydraulic path is negligible at very low frequencies. This is analytically confirmed the term $\bar{F}_{Tr}(\omega\approx 0)=\gamma_r(1+\tau_r s)\bar{X}$ results in $\gamma_r(=k_{re}(0;X)/k_{rref})=2$ with $\lambda_{kr}(0;X)$ and nominal parameters.

Schemes I and II successfully predict the dynamic force transmitted to a rigid base. Schemes III also shows good correlation except at $X=0.15$ mm. Note that the dimensionless $\bar{F}_T(\omega,X)$ estimate in fact the stiffness $\bar{K}(\omega,X)$ estimation. Overall, the linear model predicts the tendency of force well, but not the precise magnitude and phase.

5.4 Error Committed by Mechanical Model

Specifically the linear analysis of Fig. 14(a) shows a significant deviation from the experiment. Scheme IV

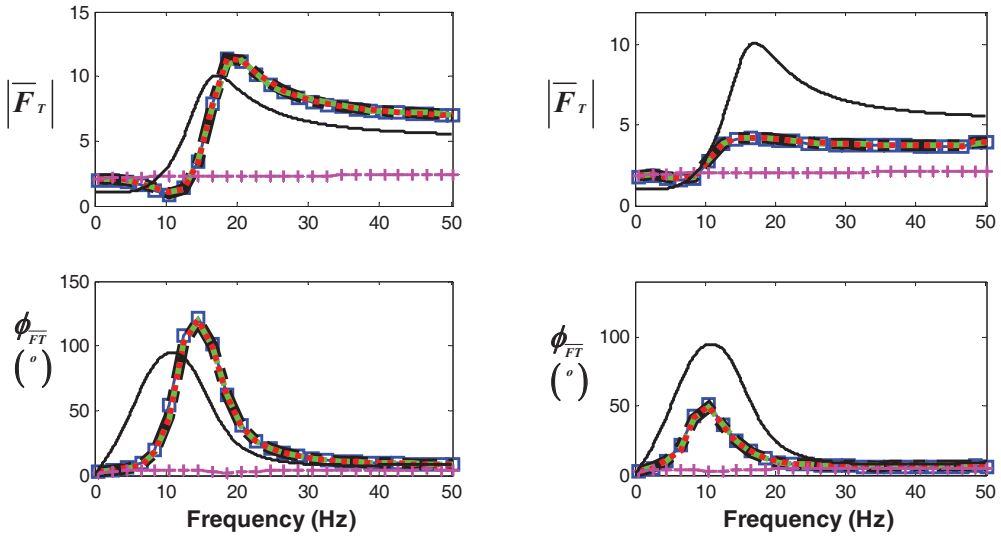

(a) *(b)*

Fig. 13—Force transmitted to the rigid base by a fixed decoupler mount: (a) X=0.15 mm; (b) X=1.5 mm. Key: ⊟ (blue), experiment; --- (black), linear model; -·- (black), Scheme I; -- (green), Scheme II; ··· (red), Scheme III; ┼ (magenta), Scheme IV.

(based on mechanical model) fails to predict the forces as all magnitude and phase values are almost constant in Figs. 13 and 14. This is investigated in Fig. 15 that compares hydraulic and rubber path forces. The error committed by scheme IV is investigated as follows where the subscript *A* implies the analogous mechanical model:

$$\bar{\varepsilon}_1(\omega,X)=\frac{\bar{F}_h(\omega,X)-\bar{F}_{Ah}(\omega,X)}{\bar{F}_h(\omega,X)}. \qquad (23)$$

When Eqns. (8a) and (8b) are incorporated in Eqn. (23), the error function (in the Laplace domain) is:

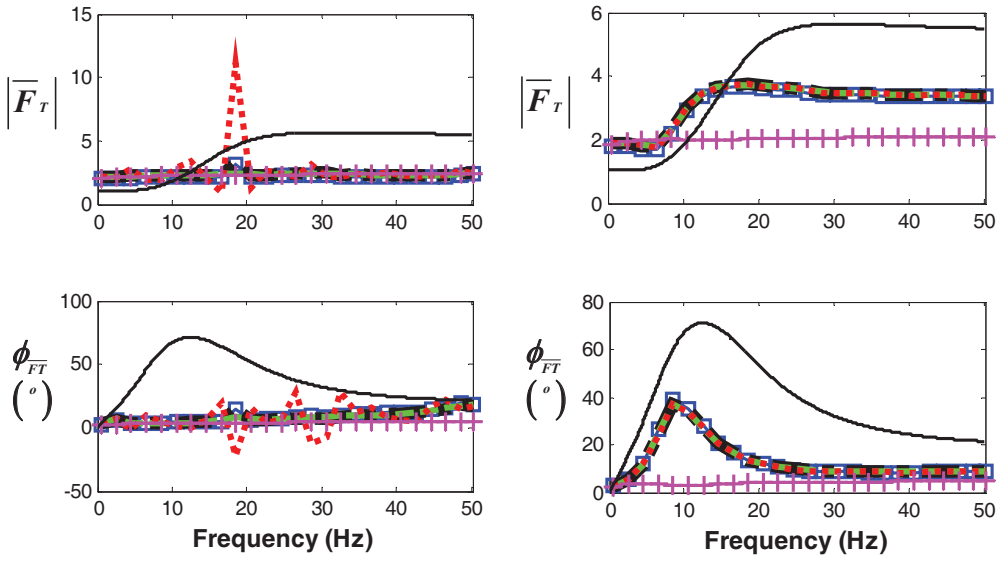

(a) *(b)*

Fig. 14—Force transmitted to the rigid base by a free decoupler mount: (a) X=0.15 mm; (b) X=1.5 mm. Key: ⊟ (blue), experiment; --- (black), linear model; -·- (black), Scheme I; -- (green), Scheme II; ··· (red), Scheme III; ┼ (magenta), Scheme IV.

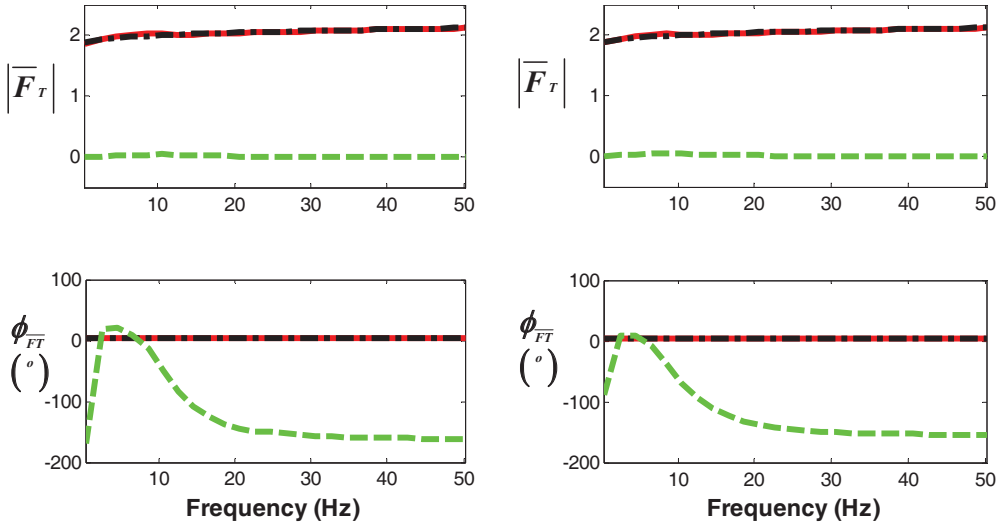

(a) *(b)*

Fig. 15—Comparison of $\bar{F}_T(\omega)$ with path contributions $\bar{F}_{Ar}(\omega)$ and $\bar{F}_{Ah}(\omega)$ using scheme IV at $X = 1.5$ mm: (a) fixed decoupler mount; (b) free decoupler mount. Key: --- (red), estimated $\bar{F}_T(\omega)$; -·- (black), estimated $\bar{F}_{Ar}(\omega)$; -- (green), estimated $\bar{F}_{Ah}(\omega)$.

$$\bar{\varepsilon}_2(s) = 1 - \frac{1}{\frac{s^2}{\omega_{N1}^2} + \frac{2\zeta_1}{\omega_{N1}}s + 1}. \quad (24)$$

Next, replace s with $j\omega$ to yield the following:

$$\bar{\varepsilon}_2(r_1) = 1 - \frac{1}{(1 - r_1^2) + i2\zeta_1 r_1}, \quad r_1 = \frac{\omega}{\omega_{N1}}. \quad (25)$$

Now we consider three cases with respect to ω_{N1}; values are 1.62 and 1.9 Hz for the fixed and free decoupler mounts, respectively. Consider the limiting case close to the zero frequency where $r_1 \to 0$:

$$\bar{\varepsilon}_2(\xi) = 1 - \frac{1}{1 + \xi i}, \quad (26a)$$

$$\xi = 2\zeta_1 r_1, \quad (26b)$$

$$|\bar{\varepsilon}_2(\xi)| = \xi/\sqrt{1 + \xi^2} \approx 0, \quad (26c)$$

$$\phi_{\bar{\varepsilon}_2} = tan^{-1}(\xi i/(1 + \xi i)) \leq 90\,^\circ. \quad (26d)$$

When $r_1 = 1$, we get:

$$\bar{\varepsilon}_2(r_1 = 1) = 1 + \frac{i}{2\zeta_1}, \quad (27a)$$

$$|\bar{\varepsilon}_2(r_1 = 1)| = \sqrt{1 + \frac{1}{(2\zeta_1)^2}} \approx 1, \quad (27b)$$

$$\phi_{\bar{\varepsilon}_2} = tan^{-1}(2\zeta_1 + i) - tan^{-1}(2\zeta_1) = tan^{-1}(2\zeta_1 + i). \quad (27c)$$

where $\phi_{\bar{\varepsilon}_2} \approx 11.53°$ (13.40°) for the fixed (free) decoupler mount by using the nominal values of ζ_1 and ω_{N1} as described in Sec. 3.

Finally consider the case when r_1 greater than 1:

$$\bar{\varepsilon}_2(r_1) = \frac{-r_1^2 + i2\zeta_1 r_1}{(1 - r_1^2) + i2\zeta_1 r_1}, \quad (28a)$$

$$|\bar{\varepsilon}_2(r_1)| = \sqrt{\frac{(-r_1^2)^2 + (2\zeta_1 r_1)^2}{(1 - r_1^2)^2 + (2\zeta_1 r_1)^2}} \approx 1, \quad (28b)$$

$$\phi_{\bar{\varepsilon}_2} = tan^{-1}\left(\frac{2\zeta_1 r_1}{-r_1^2}\right) - tan^{-1}\left(\frac{2\zeta_1 r_1}{1 - r_1^2}\right) \approx 0. \quad (28c)$$

For each case as described by Eqns. (26a)–(26d), (27a)–(27c), and (28a)–(28c), the error $|\bar{\varepsilon}_2(\omega)|$ is almost 100% over the entire range of frequencies. This confirms the chief weakness of analogous mechanical models though they have utilized[28].

5.5 Contribution of Rubber and Hydraulic Paths to the Total Force $\bar{F}_T(\omega, X)$

Figure 16 compares $\bar{F}_T(\omega, X)$ estimates based on schemes III-A, B, and C for fixed and free decoupler mounts. The results show that estimates depend upon the contribution of rubber and hydraulic paths. Scheme III-A fails to capture the precise magnitude and phase.

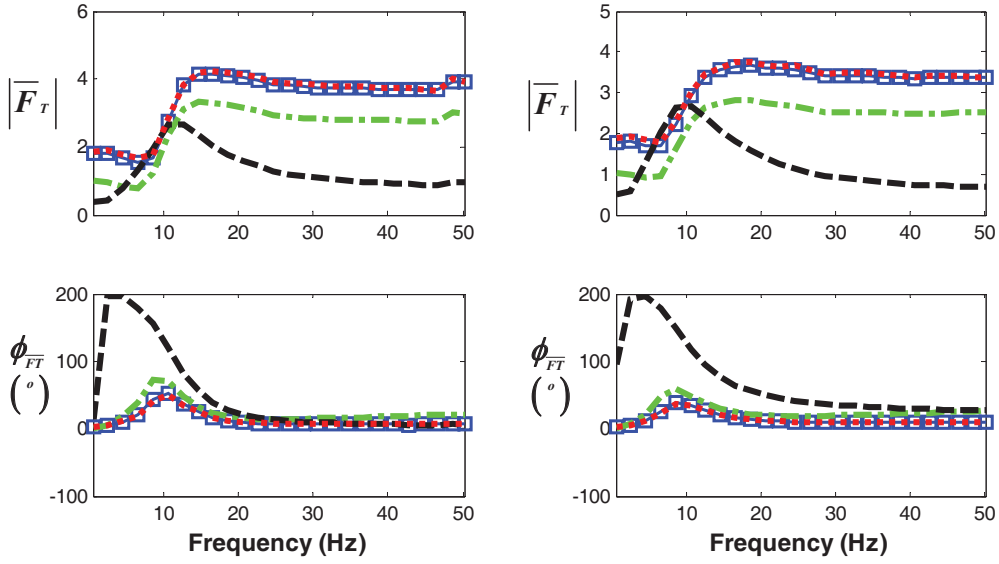

(a) *(b)*

Fig. 16—Force estimations with Scheme III at X = 1.5 mm: (a) fixed decoupler; (b) free decoupler. Key: ⊟ (blue), experiment; -·- (green), Scheme III-A; -- (black), Scheme III-B; ··· (red), Scheme III-C.

Scheme III-B shows moderate results even though the rubber path force is estimated with a quasi-linear model. Scheme III-C yields the most precise predictions when the quasi-linear models for both paths are concurrently applied. Figure 17 compares the rubber and hydraulic path forces with Scheme II with $X = 1.5$ mm. As shown in Figs. 17(a) and 17(b), $\bar{F}_T(\omega, X)$ is quite sensitive to the rubber path though rubber path forces are almost constant when compared with the hydraulic path forces.

6 DYNAMIC FORCE ESTIMATION IN TIME DOMAIN

Based upon the frequency domain results, $f_T(t)$ could be estimated in time domain by employing the following assumptions: (1) Only the steady state response is of interest under the sinusoidal displacement $x(t)$ excitation; and (2) only the mean (preload f_m) and fundamental frequency terms are considered in the Fourier expansion. As illustrated previously, the dynamic stiffness $\bar{K}(\omega)$ or force transmissibility $\bar{H}(\omega)$ could be estimated by employing $\lambda_{kr}(\omega, X)$, $\lambda_{cr}(\omega, X)$, and $\lambda_u(\omega, X)$ in the quasi-linear model. Therefore, the Fourier expansion is applied by embedding $\bar{K}(\omega)$ or $\bar{H}(\omega)$ as quasi-linear parameters with input X or P_u respectively as shown below where ω_o is the fundamental frequency:

$$f_{T\text{-}SchemeII}(t) = f_m + \chi_1 |\bar{K}(\omega_o)| sin(\omega_o t + \phi_{\bar{K}}), \tag{29a}$$

$$\chi_1 = k_{rref} X_{ref} \bar{X}. \tag{29b}$$

$$f_{T\text{-}SchemeIII}(t) = f_m + \chi_2 |\bar{H}(\omega_o)| sin(\omega_o t + \phi_{\bar{H}}), \tag{30a}$$

$$\chi_2 = k_{rref} X_{ref} |\bar{P}_u|. \tag{30b}$$

The χ_1 and χ_2 terms are used for finding the $f_T(t)$ history in force units (N) as the estimation yields the normalized values. Further, $f_{T\text{-}SchemeII}(t)$ and $f_{T\text{-}SchemeIII}(t)$ are the force estimations from Scheme II-C and III-C respectively. Figure 18 compares the time histories as predicted by Eqns. (29a), (29b), (30a), and (30b) with measured forces for the free decoupler mount at $\omega_0/2\pi = 8.5$ Hz and $X = 1.5$ mm. This result is a significant improvement over the previous formulation as illustrated in Fig. 3. When the quasi-linear models for both rubber and hydraulic force paths are employed, the estimation of $f_T(t)$ matches well with measured force specifically in terms of its amplitude. The discrepancies between the experiment and the proposed models are primarily due to the super-harmonic terms, which are not included in the current study. A future article will address this issue further with focus on the super-harmonic responses.

7 CONCLUSION

This article has proposed indirect methods to estimate dynamic forces that are transmitted to a rigid base by a fixed or free hydraulic mount. Specific contri-

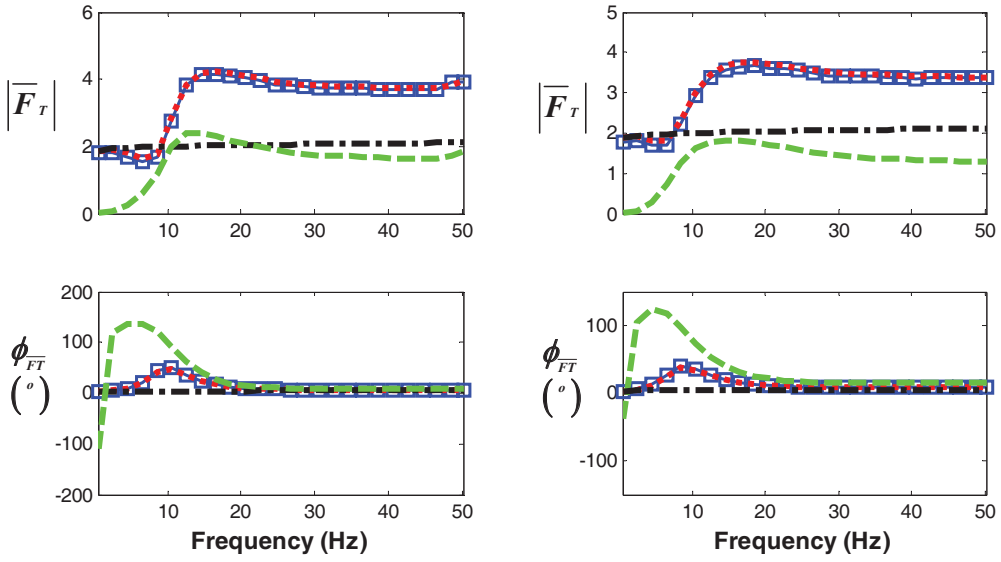

(a) (b)

Fig. 17—Comparison of $\bar{F}_T(\omega)$ with path contribution $\bar{F}_{Tr}(\omega)$ and $\bar{F}_{Th}(\omega)$ with scheme II at $X = 1.5$ mm: (a) fixed decoupler mount; (b) free decoupler mount. Key: ⊟ (blue), measured $\bar{F}_T(\omega)$; ···· (red), estimated $\bar{F}_T(\omega)$; -·- (black), estimated $\bar{F}_{Tr}(\omega)$; -- (green), estimated $\bar{F}_{Th}(\omega)$.

butions of this article include the following. First, alternate transfer function formulations are derived for a linear system that relate sinusoidal motion $x(t)$ and/or chamber pressure $p_u(t)$ to harmonic forces through rubber and hydraulic paths. In particular, the derivation of force to pressure transfer function is very promising as it permits an estimation of forces only by pressure measurements. Second, the effect of mount nonlinearities on forces is quantified only in terms of top chamber compliance and rubber path properties, unlike prior methods that need extensive models[9,13–16]. This leads to a quasi-linear model with amplitude-sensitive and spectrally-varying parameters such as $C_{ue}(\omega,X)$, $k_r(\omega,X)$ and $c_r(\omega,X)$. Since the hydraulic force path has been successfully characterized only by $C_{ue}(\omega,X)$, other hydraulic path nonlinearities such as inertia track resistance, bottom chamber compliance and decoupler flow resistance could be ignored and thus simpler force estimation schemes could be developed. Nevertheless, the rubber path of the nonlinearities must be included as well in order to accurately estimate $F_T(\omega,X)$. Third, the forces transmitted to a rigid base under harmonic displacement excitation are successfully predicted and compared with measured forces; all schemes (with a quasi-linear formulation) work well except the mechanical system model (Scheme IV) that provides almost 100% error in forces.

This article has focused on frequency domain analyses though limited results in time domain are also presented. The force time history $f_T(t)$ is predicted by applying the Fourier expansion with an embedded quasi-linear model with only the fundamental (excitation) frequency. However, force estimation methods (especially in time domain) need to include multi-harmonic response terms which are observed in measurements (Figs. 3 and 18). As part of ongoing work, the super-harmonic responses are being investi-

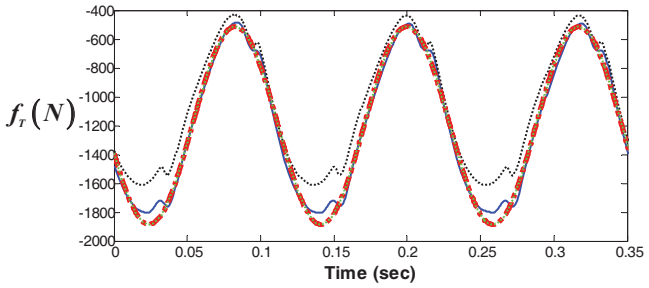

Fig. 18—Comparison between measured and predicted forces in time domain for the free decoupler mount, given sinusoidal displacement $x(t) = X \sin \omega_o t$ at $\omega/2\pi = 8.5$ Hz and $X = 1.5$ mm.. Key: — (blue), experiment; ··· (black), estimation by Eqn. (1) given nominal parameters; -· (red), estimation by Scheme II-C with quasi-linear parameters; ··· (green), estimation by Scheme III-C with quasi-linear parameters.

gated and they will be incorporated in order to better estimate the force time histories[26].

8 ACKNOWLEDGEMENT

We are grateful to the member organizations of the Smart Vehicle Concepts Center (www.SmartVehicleCenter.org) and the National Science Foundation Industry/University Cooperative Research Centers program (www.nsf.gov/eng/iip/iucrc) for supporting this work.

9 REFERENCES

1. A. Inoue, S. Kim and R. Singh, "Comparative evaluation of structure-borne noise transfer paths in a laboratory experiment", *Noise Control Eng. J.*, **54**(6), 382–395, (2006).
2. A. Inoue, R. Singh and G. A. Fernandes, "Absolute and relative path measures in a discrete system by using two analytical methods", *J. Sound Vibr.*, **313**, 696–722, (2008).
3. A. Gunduz, A. Inoue and R. Singh, "Estimation of interfacial forces in time domain for linear system", *J. Sound Vibr.*, **329**, 2616–2634, (2010).
4. Q. Leclere, C. Pezerat, B. Laulagnet and L. Polac, "Indirect measurement of main bearing loads in an operating diesel engine", *J. Sound Vibr.*, **286**, 341–361, (2005).
5. S. H. Yap and B. M. Gibbs, "Structure-borne sound transmission from machines in buildings, part 1: indirect measurement of force at the machine-receiver interface of a single and multipoint connected system by a reciprocal method", *J. Sound Vibr.*, **222**(1), 99–113, (1999).
6. R. A. Ibrahim, "Recent advances in nonlinear passive vibration isolators", *J. Sound Vibr.*, **314**, 371–452, (2008).
7. Y. Yu, N. G. Naganathan and R. V. Dukkipati, "A literature review of automotive vehicle engine mounting systems", *Mech. Mach. Theory*, **36**, 123–142, (2001).
8. R. Singh, "Rubber and hydraulic mounts: dynamic analysis, experimental characterization and vehicle vibration isolation", Course notes for the General Motors Technical Education Program, (2004).
9. S. He and R. Singh, "Estimation of amplitude and frequency dependent parameters of hydraulic engine mount given limited dynamic stiffness measurements", *Noise Control Eng. J.*, **53**(6), 271–285, (2005).
10. J. Y. Park and R. Singh, "Effect of non-proportional damping on the torque roll axis decoupling of an engine mounting system", *J. Sound Vibr.*, **313**, 841–857, (2008).
11. R. Singh, G. Kim and P. V. Ravindra, "Linear analysis of automotive hydro-mechanical mount with emphasis on decoupler characteristics", *J. Sound Vibr.*, **158**(2), 219–243, (1992).
12. J. E. Colgate, C. T. Chang, Y. C. Chiou, W. K. Liu and L. M. Keer, "Modeling of a hydraulic engine mount focusing on response to sinusoidal and composite excitations", *J. Sound Vibr.*, **184**(3), 503–528, (1995).
13. G. Kim and R. Singh, "Nonlinear analysis of automotive hydraulic engine mount", *ASME J. Dyn. Syst., Meas., Control*, **115**(3), 482–487, (1993).
14. G. Kim and R. Singh, "A study of passive and adaptive hydraulic engine mount systems with emphasis on non-linear characteristics", *J. Sound Vibr.*, **179**(3), 427–453, (1995).
15. M. Tiwari, H. Adiguna and R. Singh, "Experimental characterization of a nonlinear hydraulic engine mount", *Noise Control Eng. J.*, **51**(1), 36–49, (2003).
16. H. Adiguna, M. Tiwari, R. Singh, H. E. Tseng and D. Hrovat, "Transient response of a hydraulic engine mount", *J. Sound Vibr.*, **268**, 217–248, (2003).
17. S. He and R. Singh, "Discontinuous compliance nonlinearities in the hydraulic engine mount", *J. Sound Vibr.*, **307**, 545–563, (2007).
18. W. B. Shangguan and Z. H. Lu, "Experimental study and simulation of a hydraulic engine mount with fully coupled fluid-structure interaction finite element analysis model", *Comput. Struct.*, **82**, 1751–1771, (2004).
19. R. Fan and Z. Lu, "Fixed points on the nonlinear dynamic properties of hydraulic engine mounts and parameter identification method: Experiment and theory", *J. Sound Vibr.*, **305**, 703–727, (2007).
20. T. Q. Truong and K. K. Ahn, "A new type of semi-active hydraulic engine mount using controllable area of inertia track", *J. Sound Vibr.*, **329**, 247–260, (2010).
21. J. Christopherson and G. N. Jazar, "Dynamic behavior comparison of passive hydraulic engine mounts. Part I: Mathematical analysis", *J. Sound Vibr.*, **290**, 1040–1070, (2006).
22. J. H. Lee and R. Singh, "Nonlinear frequency responses of quarter vehicle models with amplitude-sensitive engine mounts", *J. Sound Vibr.*, **313**, 784–805, (2003).
23. J. H. Lee and R. Singh, "Existence of super-harmonics in quarter-vehicle system responses with nonlinear inertia hydraulic track mount given sinusoidal force excitation", *J. Sound Vibr.*, **313**, 367–374, (2008).
24. Acoustics and vibration—Laboratory measurement of vibro-acoustic transfer properties of resilient elements, ISO 10846: 1997, International Organization for Standardization, Geneva, Switzerland, (1997).
25. MTS Elastomer Test System 831.50, 1000 Hz model, http://www.mts.com.
26. J. Y. Yoon and R. Singh, "Dynamic force transmitted by a nonlinear hydraulic mount under sinusoidal excitation with focus on super-harmonics", Submitted to the *J. Sound Vibr.*, (2010).
27. T. C. Kim, T. E. Rook and R. Singh, "Effect of smoothening functions on the frequency response of and oscillator with clearance non-linearity", *J. Sound Vibr.*, **263**(3), 665–678, (2003).
28. J. H. Lee and R. Singh, "Critical analysis of analogous mechanical models used to describe hydraulic engine mounts", *J. Sound Vibr.*, **311**(3–5), 1457–1464, (2008).